

## Article

# An Investigation of Thermomechanical Behavior in Laser Hot Wire Directed Energy Deposition of NAB: Finite Element Analysis and Experimental Validation

Glenn W. Hatala <sup>1</sup>, Edward Reutzel <sup>2</sup>  and Qian Wang <sup>1,\*</sup>

<sup>1</sup> Department of Mechanical Engineering, The Pennsylvania State University, University Park, PA 16802, USA; gwh12@psu.edu

<sup>2</sup> Applied Research Laboratory, The Pennsylvania State University, University Park, PA 16802, USA; ewr101@psu.edu

\* Correspondence: quw6@psu.edu

**Abstract:** Laser Hot Wire (LHW) Directed Energy Deposition (DED) Additive Manufacturing (AM) processes are capable of manufacturing parts with a high deposition rate. There is a growing research interest in replacing large cast Nickel Aluminum Bronze (NAB) components using LHW DED processes for maritime applications. Understanding thermomechanical behavior during LHW DED of NAB is a critical step towards the production of high-quality NAB parts with desired performance and properties. In this paper, finite element simulations are first used to predict the thermomechanical time histories during LHW DED of NAB test coupons with an increasing geometric complexity, including single-layer and multilayer depositions. Simulation results are experimentally validated through in situ measurements of temperatures at multiple locations in the substrate as well as displacement at the free end of the substrate during and immediately following the deposition process. The results in this paper demonstrate that the finite element predictions have good agreement with the experimental measurements of both temperature and distortion history. The maximum prediction error for temperature is 5% for single-layer samples and 6% for multilayer samples, while the distortion prediction error is about 12% for single-layer samples and less than 4% for multilayer samples. In addition, this study shows the effectiveness of including a stress relaxation temperature at 500 °C during FE modeling to allow for better prediction of the low cross-layer accumulation of distortion in multilayer deposition of NAB.

**Keywords:** laser hot wire; NAB; in situ measurements; distortion; phase transformation; stress relaxation; directed energy deposition; additive manufacturing



**Citation:** Hatala, G.W.; Reutzel, E.; Wang, Q. An Investigation of Thermomechanical Behavior in Laser Hot Wire Directed Energy Deposition of NAB: Finite Element Analysis and Experimental Validation. *Metals* **2024**, *14*, 1143. <https://doi.org/10.3390/met14101143>

Academic Editor: Andrea Di Schino

Received: 30 August 2024

Revised: 3 October 2024

Accepted: 4 October 2024

Published: 8 October 2024



**Copyright:** © 2024 by the authors. Licensee MDPI, Basel, Switzerland. This article is an open access article distributed under the terms and conditions of the Creative Commons Attribution (CC BY) license (<https://creativecommons.org/licenses/by/4.0/>).

## 1. Introduction

Laser Hot Wire (LHW) Directed Energy Deposition (DED) is a type of Additive Manufacturing (AM) process capable of fabricating sizable parts with a high deposition rate [1]. In LHW DED, the wire is fed through a hot wire torch that employs Joule heating to elevate the wire temperature, then the laser melts the filler wire to deposit a bead that is fully fused to the substrate or prior deposition. As a result, the process involves dual energy inputs comprising both a laser beam as the primary heat source and Joule heating of the wire as a supplementary heat source. Compared to powder bed fusion additive manufacturing, studies on LHW DED of Nickel 625 and Ti-6Al-4V have shown that LHW enables higher build rates and is more energy efficient [2,3].

Several past studies have focused on understanding how process parameters affect LHW process stability and explored ways to improve the LHW cladding or DED processes. Shiqing et al. [4] conducted a thermal simulation for LHW DED of 304L stainless steel to determine the wire transfer stability under a set of process conditions. Later, the same group applied a similar model to investigate the wire transfer behavior and its impact on weld

formation quality for LHW cladding and welding [5]. For LHW cladding using martensitic steel, Huang et al. [6] applied the Taguchi method to select the cladding parameters, using the volumetric defect ratio as the metric to evaluate the formation quality. They found that the wire current and wire feed rate had significantly higher influence on formation quality than the laser power and scanning speed. For LHW cladding of Inconel 625, Liu et al. [7] found that the wire stability was heavily linked to the applied voltage, with arcing becoming more prevalent at higher voltages. It was observed that arcing produced sizable quantities of spatter, resulting in reduced process stability and controllability of the bead geometry. Zhang et al. [8] conducted an experimental study on LHW cladding of a cobalt-based metal-cored wire. Their study showed that while the resistive heating on the wire plays a dominant role in affecting the stability of the deposition process, the clad height, wetting angle, and dilution rates are all affected by the wire feed rate and scanning speed. The microhardness of the cladding was mainly determined by the dilution rate. Tyralla and Seefeld [9] demonstrated that the deposition rate for LHW cladding could be increased without increasing the dilution rate by making the beam perpendicular to the wire. Akbari et al. [10] showed that for a LHW DED process, increasing laser power led to reduced bead height but increased bead width, while increasing wire feed speed had the opposite effect on bead geometry. In addition, adding a lead-in and lead-out distance for deposition together with retracting the laser head away from the component at a higher speed near the end of the bead was found to improve build quality [11].

One challenge that remains prevalent for LHW DED involves the excessive distortion developed during component fabrication. Nie et al. [12] conducted a thermomechanical simulation for LHW deposition of H13 steel, where the temperature and stress–strain fields and resulting distortion were computed using ABAQUS Finite Element (FE) software. Predictions of the temperature evolution at several selected locations were validated using in situ thermocouple measurements. The relative errors between simulated temperatures and experimental measurements were up to 25%. Displacement along the side edge of the part was measured for comparison with the FE prediction results. The relative errors of the simulated displacements with respect to the experimental measurements were up to 30%. Liu et al. [13] applied FE simulations to study the effect of the hot wire on the temperature field and residual stress distribution for laser hot wire welding with A36 steel plates and ER70S-6 steel wire. An X-Ray Diffraction (XRD) technique was used to validate the residual stress prediction at the top surface of the weld bead. Their results suggested that lowering the hot wire voltage can help reduce the residual stress occurring in the weld pool. Liang et al. [14] presented simulation results from a fluid mechanical model of stress evolution in wire feeding AM of Ti-6Al-4V, although without experimental validation. Their model was able to show the effect of molten-pool morphologies on stress and suggested that the surface-forming quality can influence the residual stress. Yao et al. [15] conducted a 3D uncoupled thermomechanical FE analysis for laser hot wire cladding of multitrack 316L stainless steel coatings using ANSYS. Their thermal model was calibrated through thermocouples. The model predicted transverse and longitudinal residual stress distributions at the cladding surface as well as at the substrate, which were validated through XRD measurements. The model predictions for the longitudinal residual stress showed good agreement with measurements; however, there were substantial discrepancies between the transverse stress predictions and the measurements, indicating room for model improvement to reduce simulation errors.

Note that none of the aforementioned thermomechanical simulations studied LHW DED of Nickel Aluminum Bronze (NAB) alloys, which are used for parts in many maritime applications due to their superior mechanical properties and corrosion resistance. There has been increasing interest in shifting from the traditional casting approach to manufacturing NAB parts through laser-based AM processes [16]. Additive manufacturing of NAB alloys has been found to provide increased yield strength and corrosion resistance compared to cast counterparts; see the review papers [17,18] and references therein. These improved properties are primarily attributed to the increased cooling rates associated with laser-based

AM processes relative to traditional casting, which leads to lower presence of intermetallic phases in the as-built samples compared to the cast material [19]. Postprocess heat treatments have also been demonstrated to improve corrosion resistance of as-built NAB alloys [20,21]. In our prior study [22], temperature-dependent thermal and mechanical material properties of NAB C95800 were experimentally measured and subsequently used in a preliminary thermomechanical analysis without experimental validation.

In this paper, an experimental study is conducted to investigate the thermomechanical behavior in LHW DED of NAB builds for both single-layer and multilayer test coupons. In situ measurements of temperature histories at multiple locations in the substrate as well as the displacement history at the free end of the cantilevered substrate are used to validate the finite element predictions. It is worth pointing out that compared to the aforementioned thermomechanical studies for LHW DED of steel alloys [4,5,12,13], NAB alloys exhibit different microstructures and phase transformations, which affect the resulting residual stress and distortion. Moreover, unlike our earlier analysis in [22], an additional novelty of the finite element modeling in this study is that it accounts for the effect of NAB's phase transformations on the residual stress by including a stress relaxation temperature at 500 °C, which allows the resulting predictions to reach good agreement with the distortion measurements.

## 2. Methods and Materials

### 2.1. LHW DED Process

Figure 1 illustrates the experimental setup, including a robotic LHW DED system and a substrate clamped on one side. The robotic LHW is composed of a six-axis ABB IRB-6700 150/3.2 robot (ABB, Zurich, Switzerland) along with an ABB IRBP A-750/1450 two-axis work piece positioner (ABB, Zurich, Switzerland). The energy input makes use of a YLR-12000-C IPG Photonics Ytterbium fiber laser (IPG Photonics, Oxford, MA, USA) (1070 nm wavelength) combined with 200  $\mu\text{m}$  process fiber. The output energy is collimated and focused using  $f = 150$  mm and  $f = 600$  mm water-cooled reflective parabolic mirrors. During processing, the beam was defocused by processing approximately 115 mm past focus, resulting in an approximate beam diameter of 3.9 mm (as extrapolated from beam caustic measurement taken at focus). A Lincoln Electric Power Wave<sup>®</sup> R500 and STT<sup>®</sup> control module (both from Lincoln Electric, Cleveland, OH, USA) are used to prevent arc initiation. In this study, the LHW system used a Laser Mechanisms FiberSCAN HR laser processing head (Laser Mechanisms, Novi, MI, USA) that oscillates the laser beam at 7.5 Hz with a beam scanning width of 3.1 mm perpendicular to the build direction.

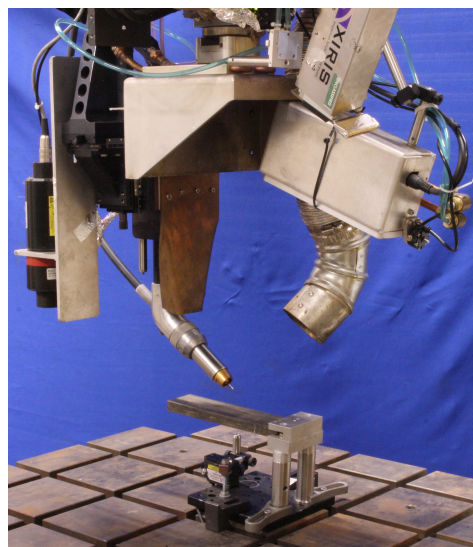


**Figure 1.** Experimental setup, including robotic LHW DED system and clamped substrate.

For each deposited bead, the LHW system employs a five-stage process consisting of pre-heating, pre-filling, main deposition, end-filling, and end-delay. Table 1 summarizes the laser power, wire feed rate, and time duration of each stage used in this study. These process parameters were developed in previous experiments to reliably produce depositions with no observable lack of fusion and minimal gas porosity [22]. The pre-heating stage employs the laser to heat the substrate or previous layer before depositing any wire. In this stage, the robot arm does not move and the laser simply oscillates at the specified frequency. In the pre-filling stage, the robot arm remains stationary with the oscillating laser and the wire feed is initiated. In the main deposition phase, the wire feed rate increases and the robot arm moves along the path of the bead at the default travel speed of 7 mm/s. At the end of the bead, corresponding to end-filling phase, the robot arm ceases movement and the wire continues to deposit at a lower rate. Last, during the end delay phase, the laser power drops and the wire stops feeding into the bead, finishing the process.

**Table 1.** Process parameters of each processing stage [22].

Stage	Wire Feed Rate	Laser Power	Laser Travel Speed	Stage Duration
Pre-Heating	0 mm/s	9 kW	-	0.2 s
Pre-Filling	37.5 mm/s	9 kW	-	0.1 s
Main Deposition	60 mm/s	9 kW	7 mm/s	Determined by bead length
End-Filling	45 mm/s	6.5 kW	-	0.1 s
End-Delay	0 mm/s	2 kW	-	0.5 s

The hot-wire supply in this study operates with an average current of 100 A at a voltage of 2.26 V, with a wire diameter of 1.14 mm. The wire length with current applied (from contact tip to melt pool) is 22.5 mm. These parameters are summarized in Table 2.

**Table 2.** Hot wire parameters.

Current Supplied	100 A
Average Voltage	2.26 V
Wire Diameter	1.14 mm
Wire Length with Current Applied	22.5 mm

## 2.2. NAB Alloys

Temperature-dependent material properties for NAB alloys were obtained in our prior work [22] from measurements on test specimens fabricated by LHW DED using feedstock material complying with MIL-CuNiAl wire requirements and a C63200 substrate material defined by ASTM B150 [23]. Measurements of the chemical composition of the as-built LHW DED specimens of NAB are provided in Table 3. The temperature-dependent material properties, including thermal diffusivity, specific heat, and thermal conductivity, are provided in Table 4. The temperature-dependent mechanical properties, including the coefficient of thermal expansion, Young's modulus, and yield strength, are provided in Table 5. Table 6 lists several other parameters of NAB, where the NAB density at room temperature is taken from [22] and other properties from C98500 Cast NAB [24].

**Table 3.** NAB chemical composition of as-built LHW DED test specimens [22].

Composition (wt.%)	Cu	Fe	Ni	Al	Mn	Si
MIL-CuNiAl in experiment	81.7	3.29	5.40	8.67	0.81	0.11
MIL-E-23765/3A (type MIL-CuNiAl)	Remainder	3.00–5.00	4.00–5.50 <sup>a</sup>	8.50–9.50	0.60–3.50	– <sup>b</sup>

<sup>a</sup> Nickel including Cobalt; <sup>b</sup> Total other elements not exceeding 0.50.

**Table 4.** NAB thermal properties [22].

Temperature [°C]	Thermal Diffusivity [m <sup>2</sup> /s]	Specific Heat [J/(kg·K)] × 10 <sup>3</sup>	Thermal Conductivity [W/(m·K)] × 10 <sup>2</sup>
23	0.104	0.433	0.341
50	0.112	0.440	0.371
100	0.126	0.453	0.430
200	0.147	0.473	0.525
300	0.163	0.477	0.586
400	0.178	0.525	0.704
500	0.189	0.538	0.766
600	0.197	0.478	0.822
700	0.179	0.639	0.865
800	0.157	0.705	0.839
900	0.130	0.936	0.714
950	0.116	0.736	0.643

**Table 5.** NAB mechanical properties [22].

Temperature [°C]	Coeff. of Thermal Expansion [1/°C]	Young's Modulus [GPa]	Yield Strength [MPa]
23	11.2	122	410
100	19.6	128	399
200	22.0	127	393
300	23.7	104	389
400	25.5	92.7	320
500	27.0	73.4	167
600	28.5	35.9	109
700	30.3	21.7	57.9
800	31.5	8.27	25.2
900	33.8	n/a	n/a

**Table 6.** Other NAB properties [22,24].

Parameter	Value	Unit
Density	7.550	kg/m <sup>3</sup>
Latent Heat of Fusion	230	kJ/kg
Solidus Temperature	1043	°C
Liquidus Temperature	1060	°C
Electrical Conductivity	7	% IACS
Electrical Resistivity	$2.428 \times 10^{-7}$	$\Omega \cdot m$

### 2.3. Experimental Design

A series of MIL-CuNiAl wire-fed coupons, including both single-layer and multilayer samples, were built on C63000 NAB substrates to validate the temperature and distortion predictions. Two repeated samples were fabricated for each type of build. Figure 2 shows the dimensions of the substrate and the single-layer part with a layer height of 1.9 mm. The multilayer part consists of three layers with a total height of 5.7 mm. The other dimensions of the multilayer part and the dimensions of the substrate are the same as for the single-layer part. Figure 3 shows the experimental setup for in situ temperature and deflection measurements on the substrate. One side of the substrate is clamped with a torque of 15 ft-lbs into an aluminum clamping fixture, whereas the opposite side is allowed to move freely in the vertical z-direction during the build process.

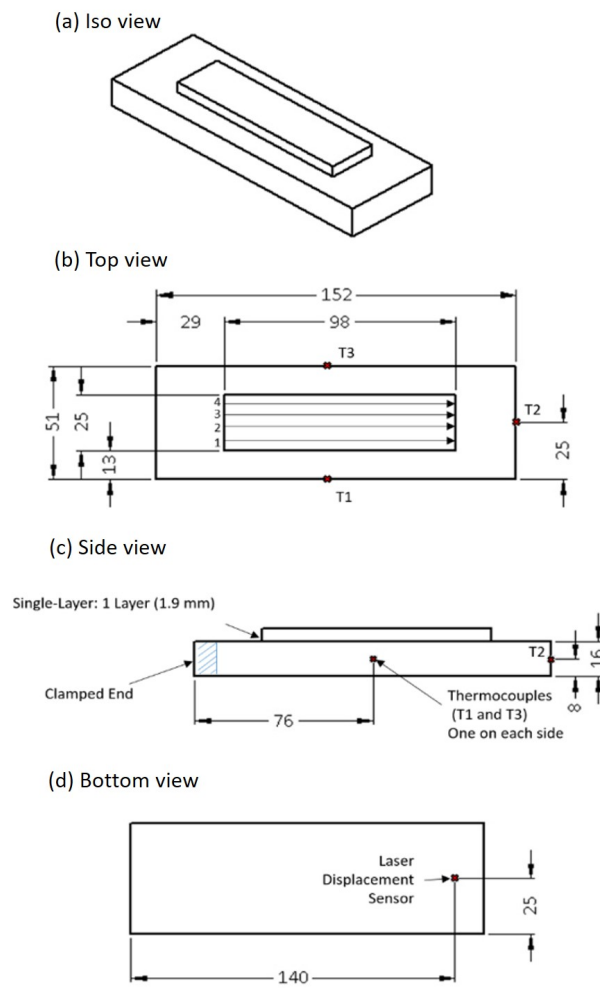


**Figure 2.** Single-layer part dimensions. All measurements are in mm; T1–T3 denote the thermocouples at three locations on the substrate.

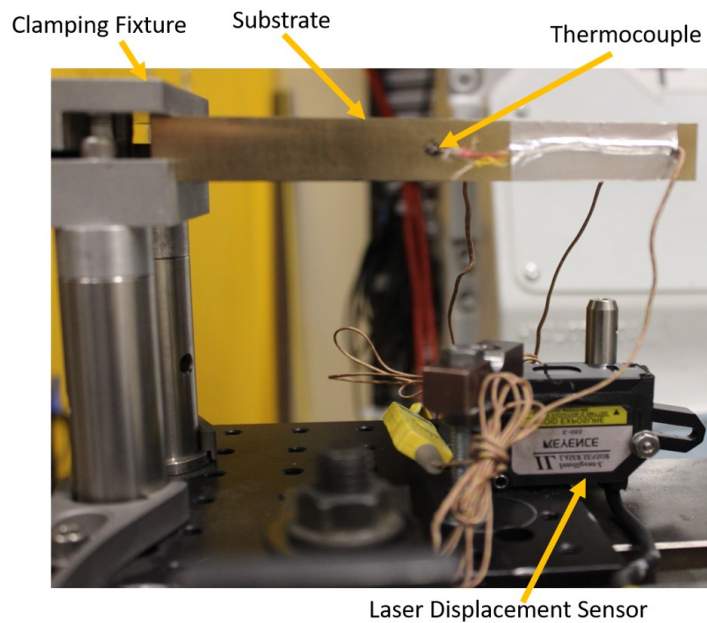


**Figure 3.** In situ sensing setup for thermal and mechanical measurements.

Each single-layer sample consisted of four unidirectional beads with a hatch spacing of 5.6 mm. A 5 s inter-pass dwell time allowed for movement of the laser head from bead to bead. Each multilayer sample consisted of three layers, with each layer fabricated in the same way as the single-layer samples. The deposition sequence for the unidirectional beads was from 1–4 on odd layers and in reverse order from 4–1 on even layers. After depositing each layer, the laser head was moved up in the z-direction by 1.9 mm to deposit the next layer, with an interlayer dwell time of 24 s. After the entire build was completed, the part was allowed to cool and freely distort before being removed from the clamp.

In situ temperature was measured at three locations on the substrate, denoted as T1–T3, using Type K Thermocouples with a temperature range of  $-200\text{ }^{\circ}\text{C}$  to  $1260\text{ }^{\circ}\text{C}$  and measurement accuracy of  $\pm 2.2\text{ }^{\circ}\text{C}$ . As illustrated in the top and side views of Figure 2, T1 and T3 were located at the midpoint of the longer side of the substrate, whereas T2 was located at the midpoint of the shorter side of the substrate. All thermocouples were placed at middle depth of the substrate on the outside surface. Thermocouple data were recorded using a National Instruments cRIO-9039 controller (National Instruments, Austin, TX, USA) with the National Instruments 9213 temperature input module. As shown in the bottom view of Figure 2, in situ deflection was measured at the bottom surface of the substrate using a KEYENCE IL-650 laser displacement sensor (LDS) (Keyence Corporation of America, Elmwood Park, NJ, USA) with a measurement accuracy of 2 microns; see Figure 3.

A laser power of 9 kW was used for deposition on the substrate under ambient temperature of  $25\text{ }^{\circ}\text{C}$  with a laser travel speed of 7 mm/s. Other laser and hot wire parameters are respectively provided in Tables 1 and 2 in Section 2.1.

## 2.4. Finite Element Modeling

### 2.4.1. Thermal Model

Thermal simulation of the LHW DED process was conducted by solving the following heat transfer energy balance, which has been widely used in thermal modeling for AM processes [25]:

$$\rho C_p \frac{\partial T}{\partial t} = -\nabla \cdot \mathbf{q}(\mathbf{x}, t) + Q(\mathbf{x}, t) \quad (1)$$

where  $\rho$  is the mass density,  $C_p$  is the temperature-dependent specific heat,  $T$  is the temperature field,  $\mathbf{q}$  is the heat flux vector,  $\mathbf{x}$  denotes the position vector, and  $Q$  denotes the volumetric internal heat generation rate. The heat flux vector satisfies

$$\mathbf{q}(\mathbf{x}, t) = -k\nabla T, \quad (2)$$

where  $k$  is the temperature-dependent thermal conductivity and  $\nabla = [\frac{\partial}{\partial x} \quad \frac{\partial}{\partial y} \quad \frac{\partial}{\partial z}]^T$ , with  $x$ ,  $y$ , and  $z$  representing the Cartesian spatial coordinates and  $[\cdot]^T$  denoting the matrix transpose. The surface heat loss due to convection can be computed as

$$q_{conv} = h(T_s - T_a), \quad (3)$$

where  $T_s$  is the surface temperature,  $T_a$  is the ambient temperature, and  $h$  is the convection coefficient. The surface heat loss due to radiation can be computed as

$$q_{rad} = \varepsilon \sigma_{sb} (T_s^4 - T_a^4), \quad (4)$$

where  $\varepsilon$  is the surface emissivity and  $\sigma_{sb}$  denotes the Stefan–Boltzmann constant.

The heat source  $Q$  is described using the double ellipsoid model by Goldak et al. [26]:

$$Q = \eta P \frac{6\sqrt{3}}{abc\pi\sqrt{\pi}} e^{-[\frac{3x^2}{a^2} + \frac{3y^2}{b^2} + \frac{3(z+vt)^2}{c^2}]} \quad (5)$$

where  $\eta$  denotes the laser absorption efficiency; the variables  $x$ ,  $y$ , and  $z$  are coordinates of the laser heat source;  $a$ ,  $b$ , and  $c$  are the transverse, depth, and longitudinal dimension of the ellipsoid, respectively; and  $v$  is the laser scan speed. The total power  $P$  consists of two components

$$P = P_{laser} + P_{wire}, \quad (6)$$

where  $P_{laser}$  is the laser heat power and  $P_{wire}$  is the equivalent heat power from Joule heating generated by the hot wire.  $P_{wire}$  can be computed as follows:

$$P_{wire} = q_{wire} \cdot S \cdot L \quad (7)$$

where  $S$  is the wire's cross-sectional area and  $L$  denotes the length of the wire with applied current, which corresponds to the distance from the end of the contact tip to the melt pool. The variable  $q_{wire}$  denotes the heat flux from the resistance heating produced by the hot wire:

$$q_{wire} = \frac{I^2 \cdot \rho_r}{S^2} \quad (8)$$

where  $I$  is the current applied to the wire and  $\rho_r$  denotes the resistivity of the wire material, which in this study is NAB. The hot wire parameters used in the simulations are provided in Table 2, while the temperature-dependent specific heat and conductivity of the NAB used for the thermal analysis are provided in Table 4.

#### 2.4.2. Mechanical Model

The results from the thermal analysis were then used as inputs for the quasi-static mechanical analysis. The stress equilibrium is governed by the following equation:

$$\nabla \cdot \sigma = \mathbf{0} \quad (9)$$

where  $\sigma$  is the stress, satisfying the mechanical constitutive law

$$\sigma = \mathbf{C}\epsilon_e, \quad (10)$$

where  $\mathbf{C}$  denotes the fourth-order isotropic material stiffness tensor. For small deformations, the total strain  $\epsilon$  is computed as the sum of the elastic strain  $\epsilon_e$ , plastic strain  $\epsilon_p$ , and thermal strain  $\epsilon_T$ :

$$\epsilon = \epsilon_e + \epsilon_p + \epsilon_T. \quad (11)$$

The thermal strain can be computed as follows:

$$\epsilon_T = \alpha(T - T_{ref}) [ 1 \ 1 \ 1 \ 0 \ 0 \ 0 ]^T \quad (12)$$

where  $\alpha$  is the coefficient of thermal expansion and  $T_{ref}$  is the reference temperature, which in this study is set to 25 °C. The plastic strain  $\epsilon_p$  is computed through the von Mises yield criterion and the Prandtl–Reuss flow rule:

$$f = \sigma_m - \sigma_y(\epsilon_q, T) \quad (13)$$

$$\dot{\epsilon}_p = \dot{\epsilon}_q \mathbf{b} \quad (14)$$

$$\mathbf{b} = \left( \frac{\partial f}{\partial \sigma} \right)^T \quad (15)$$

where  $f$  is the yield function,  $\sigma_m$  is the von Mises stress,  $\sigma_y$  is the yield strength,  $\epsilon_q$  is the equivalent plastic strain,  $\mathbf{b}$  is the flow vector, and  $\dot{\epsilon}_p$  and  $\dot{\epsilon}_q$  are the plastic strain rate and equivalent plastic strain rate, respectively.

The stress and strain can be computed in an incremental way from the  $(k - 1)$ th step to the  $k$ th step, as follows:

$$\sigma^{(k)} = \sigma^{(k-1)} + \Delta\sigma, \quad (16)$$

$$\epsilon^{(k)} = \epsilon^{(k-1)} + \Delta\epsilon. \quad (17)$$

Per Equation (10),  $\Delta\sigma$  can be calculated as follows:

$$\begin{aligned} \Delta\sigma &= \Delta C \epsilon_e^{(k-1)} + C \Delta\epsilon_e \\ &= \Delta C (\epsilon^{(k-1)} - \epsilon_p^{(k-1)} - \epsilon_T^{(k-1)}) \\ &+ C (\Delta\epsilon - \Delta\epsilon_p - \Delta\epsilon_T). \end{aligned} \quad (18)$$

The thermal strain increment  $\Delta\epsilon_T$  and plastic strain increment  $\Delta\epsilon_p$  can be computed through Equations (12)–(15).

### 2.4.3. Hypothesis on Stress Relaxation Due to Phase Transformations

In the solidification process of NAB alloys, a Body-Centered Cubic (BCC)  $\beta$  phase forms at high temperatures, then transforms to a Face-Centered Cubic (FCC)  $\alpha$  phase with various  $\kappa$  precipitates, and finally enters the  $\gamma_2$  intermetallic phase during cooling [17]. Pisarek [27] divided the crystallization and phase transformations during the solidification process of 11Al-6Ni-5Fe-1Mn NAB alloy into stages I–VIII, with each stage corresponding to a different temperature range. Stages I–III describe the solidification, starting from the liquidus temperature and followed by formation of the  $\beta$  solid solution. The  $\kappa_2$  precipitate starts at stage IV, with the temperature  $T$  reduced from 985 °C to 890 °C. The  $\beta \rightarrow \beta + \alpha$  transformation mainly occurs in Stage V (945 °C >  $T$  > 760 °C). In the last stage (stage VIII), corresponding to 515 °C >  $T$  > 460 °C, the remaining  $\beta$  transforms to  $\alpha + \gamma_2$ . Note that the microstructure of NAB can be sensitive to the alloy's chemical composition and the magnitude of the cooling rate [27,28]. The review paper by Orzolek et al. [17] points out that, for modern NAB alloys with a lower Al wt.%, when the temperature falls between 400–600 °C with a high cooling rate, the  $\beta$  phase transforms to the partially ordered  $\beta_1$  phase instead of to the  $\gamma_2$  intermetallic phase described by Pisarek [27]. Under further cooling to about 200 °C, the  $\beta_1$  phase transforms to the martensitic phase  $\beta'$ .

In terms of the dilatometry curves for Cu-12Al provided in Figure 4, the dimensional change rate is about 8% around 500 °C, where  $\beta \rightarrow \beta_1$ . In contrast, around 200 °C, where the martensitic transformation  $\beta \rightarrow \beta'$  occurs, the dimensional change rate is about 2%, which is only one quarter of its counterpart associated with the phase transformation  $\beta \rightarrow \beta_1$  at 500 °C, and as such is considered non-significant. Therefore, we hypothesize that during cooling, the transformation strains due to phase transformations at 500 °C and above will be significant enough to be accounted for in the FE modeling.

We further hypothesize that the significant transformation strains above 500 °C for NAB will counteract the thermal contraction strains [29], resulting in residual stress relaxation. In computing the iteration of stress and strain in Equations (16)–(18), the following equations are set:

$$\epsilon_e^{(k-1)} = 0, \quad \text{i.e.,} \quad \sigma^{(k-1)} = 0, \quad (19)$$

$$\epsilon_q^{(k-1)} = 0. \quad (20)$$

The threshold temperature where Equations (19) and (20) are enforced is referred to as the stress relaxation temperature. A similar stress relaxation modeling was employed in [30] for Ti-6Al-4V at temperatures exceeding 690 °C to predict distortion in the directed energy deposition of Ti-6Al-4V parts, where the FE predictions showed good agreement with the experimental measurements of distortion.

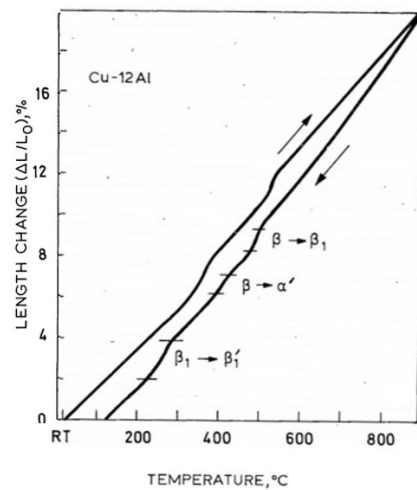


**Figure 4.** Dilatometry curve illustrating the volumetric change in microstructural transformations for Cu-12Al during a heating and cooling cycle [28].

#### 2.4.4. Laser Path Model

Following our preliminary study [22], the triangular laser path in the physical system of the LHW DED was simplified into a straight path using the same linear heat input. Specifically, a larger heat source with a 9 mm bead width was used to replace the 3.9 mm diameter oscillating laser from the physical system. This straight-path heat source of 9 mm diameter uses the same total energy per unit length over the same amount of time as the oscillating laser. Such simplification was shown to result in a significant improvement in computation efficiency for single-layer deposition at the cost of about a 5.3% error in the predicted temperatures compared to the simulated temperatures using the oscillating laser for several locations on the substrate [22].

#### 2.4.5. Numeric Implementation

The FE software PanX from PanOptimization LLC was used for the thermomechanical simulations. The material deposition was modeled through a hybrid of quiet and inactive elements activated as the added material solidifies [31]. The thermomechanical analysis was sequentially coupled at the layer level. At a layer  $i$ , the thermal analysis was run first, followed by the mechanical analysis for layer  $i$ , then the two-step thermomechanical analysis was repeated for layer  $i + 1$ . Table 7 lists the meshing and time step parameters used in the simulation. A prior mesh convergence study for a laser cladding process [32] evaluated meshes based on two, three, and four elements per laser diameter, and showed that the error between the coarsest mesh (using two elements) and finest mesh (using four elements) was 3.3%. In this study, our mesh convergence analysis for LHW AM of NAB indicated that the difference between using three and using four elements per laser diameter was 1.8%; thus, three elements per laser diameter was chosen in order to balance the prediction accuracy and computation cost.

**Table 7.** Meshing and time step parameters in FE simulations.

Elements per laser diameter	3
Minimum number of fine layers beneath heat source	8
Number of refinement levels	3
Dimensionless time tolerance	2.5
Maximum allowable time increment	10 s
Minimum allowable time increment	$10^{-5}$ s

The number of fine layers beneath the heat source was set to 8, while the number of refinement levels was set to 3 to ensure sufficient computation accuracy for temperature,

stress, plastic strain, and distortion, as suggested by [33] for an Octree mesh coarsening strategy. Adaptive time steps were used, where smaller time increments were employed during laser heating in order to provide adequate accuracy, while larger time increments were applied when there was no laser heating in order to reduce computational load. The minimum allowable time increment was set at  $10^{-5}$  s, while the smallest time step observed in the simulation was on the order of  $10^{-3}$  s, where convergence was reached. The maximum allowable time increment was set to 10 s. Note that with adaptive time steps the maximum time increment of 10 s was only used while simulating cooling, where the resulting temperature and displacement vary rather slowly compared to during laser processing and as such they do not require high temporal resolution. Decreasing the maximum allowable time increment will cause unnecessary computational cost during the cooling period.

For simulation of a multilayer part, Figure 5 shows the meshing used at the start of the deposition process and at the end of the process, where the mesh coarsens at the bottom of the substrate throughout deposition. As there are enough fine layers beneath the active laser (see Table 7), the added material from the deposition does not coarsen throughout the build. The total number of elements and number of nodes used in the FE simulations are provided in Table 8.

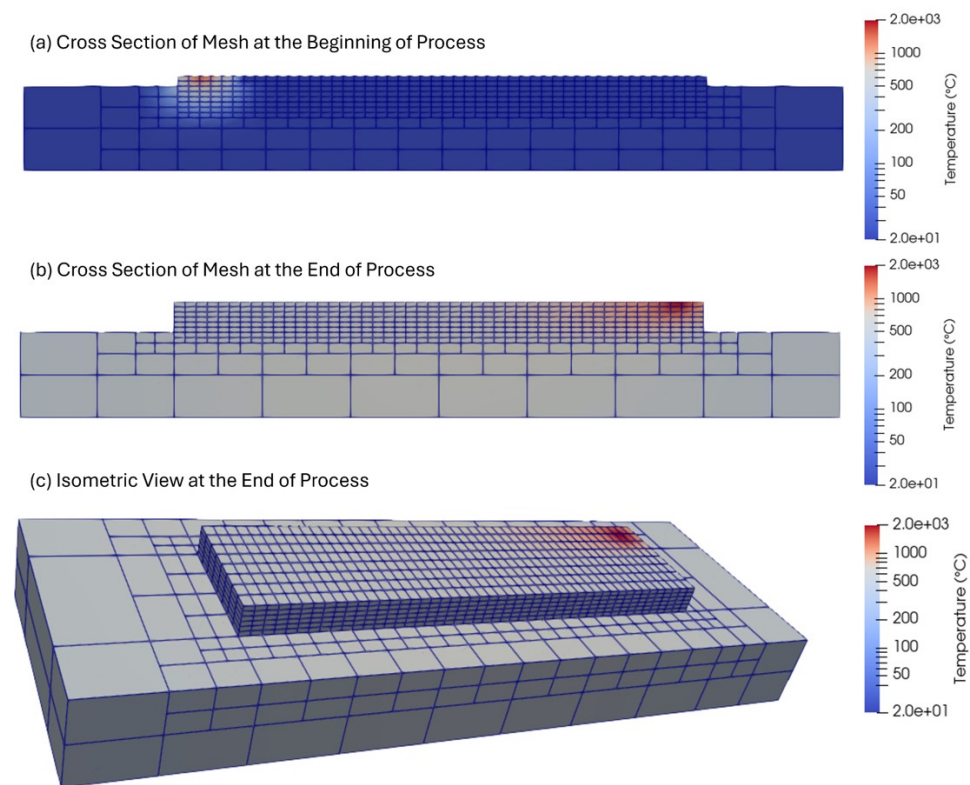


**Figure 5.** Meshing used in the simulation of a multilayer build.

**Table 8.** Number of elements and nodes in FE simulations.

Model	Number of Elements	Number of Nodes
Single-layer simulation	3964	5168
Multilayer simulation	5500	6932

### 3. Results and Discussion

Figure 6 shows images of the final builds. In this section, FE model parameters such as the optical laser absorptivity and global convection coefficient are first calibrated using the FE predicted temperature histories at TC1–TC3 versus the in situ measurements from

the single-layer coupon. Table 9 shows the results of a parametric study with respect to combinations of various sample values of laser efficiency and convection coefficients evaluated in terms of a metric on the temperature prediction error. At the location of each thermocouple (TC1–TC3), the maximum percentage of temperature error for FE prediction is computed as follows:

$$e_T = \max_i \left| \frac{T_i^s - T_i^m}{T_i^m} \right| \times 100\% \quad (21)$$

where  $T_i^s$  and  $T_i^m$  respectively represent the FE-simulated and in situ measured temperatures at time instant  $i$ . The entire time history of the recorded data is considered.

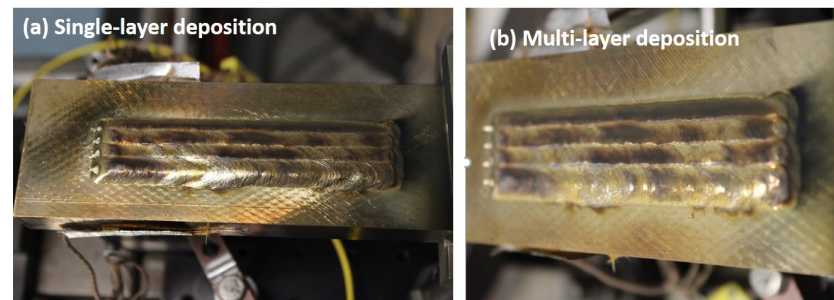


Figure 6. Images of sample depositions.

Table 9. Parametric study for single-layer temperature prediction.

Convection (W/(m <sup>2</sup> K))	Laser Absorptivity	TC1 Max %Error	TC2 Max %Error	TC3 Max %Error
30	0.15	12%	11%	15%
	0.20	6%	7%	8%
	0.25	15%	14%	14%
35	0.15	10%	15%	17%
	0.18	4%	10%	9%
	<b>0.19</b>	<b>3%</b>	<b>5%</b>	<b>5%</b>
	0.20	4%	9%	9%
40	0.25	12%	14%	16%
	0.15	11%	17%	20%
	0.20	4%	12%	13%
	0.25	14%	15%	18%

This parametric study of single-layer temperature predictions led us to choose the coefficient of laser absorptivity  $\eta = 0.19$  and a convection coefficient of 35 W/(m<sup>2</sup> K), providing relatively small prediction errors across all three thermocouples. The selected  $\eta$  value falls within the suggested range of 0.10–0.30 for the laser absorptivity provided in [12]. The selected parameters for the laser absorptivity and convection coefficient are then used to generate the mechanical simulation for the single-layer samples. Finally, these parameters are employed in the thermomechanical simulations for multilayer samples evaluated using experimental measurements.

### 3.1. Single Layer

Figure 7a shows the FE predicted temperature history at TC1–TC3, while Figure 7b shows the substrate deflection (distortion) histories at the location of LDS predicted by the FE model accounting for the stress relaxation and the FE model without stress relaxation. The shaded areas indicate the laser's active time in depositing each bead. It can be observed that the FE predicted temperatures show good agreement with the measurements. It is notable that the prediction difference for substrate deflection between the two FE models with or without stress relaxation is minimal for single-layer deposition. For either FE model, the predicted substrate deflection during laser deposition has a similar trend and

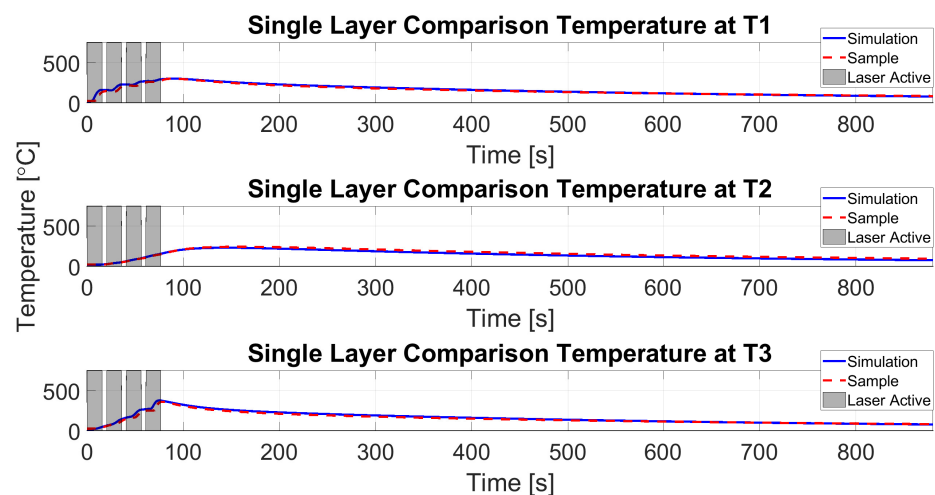
shape to the in situ measurements, although there is some over-prediction for the final steady-state distortion.

We further define a metric for evaluating the FE prediction errors with respect to the substrate deflection. Specifically, the percentage of the final displacement error  $e_D^f$  for FE prediction at the location of LDS is computed for all time instants  $t_i$  in the final 30 s of the recorded data:

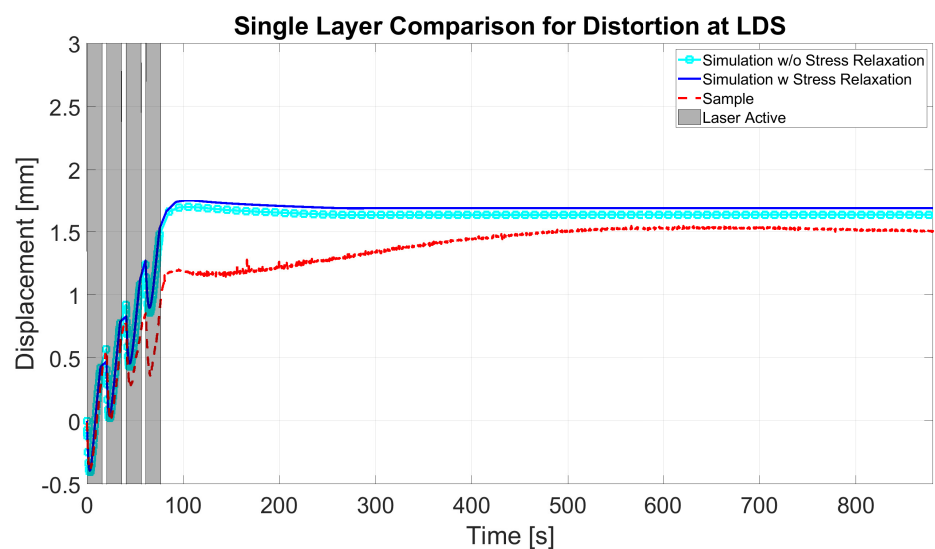
$$e_D^f = \frac{1}{N} \sum_i \left| \frac{D_i^s - D_i^m}{D_i^m} \right| \times 100\% \quad (22)$$

where  $D_i^s$  and  $D_i^m$  denote the FE-simulated and measured displacement at the LDS location for each time instant  $t_i$ , while  $N$  denotes the total number of sampling points included.

The prediction error for the final distortion  $e_D^f$  is about 12% for the single-layer deposition, indicating reasonable agreement between the FE prediction and measurements.



(a) Temperature history

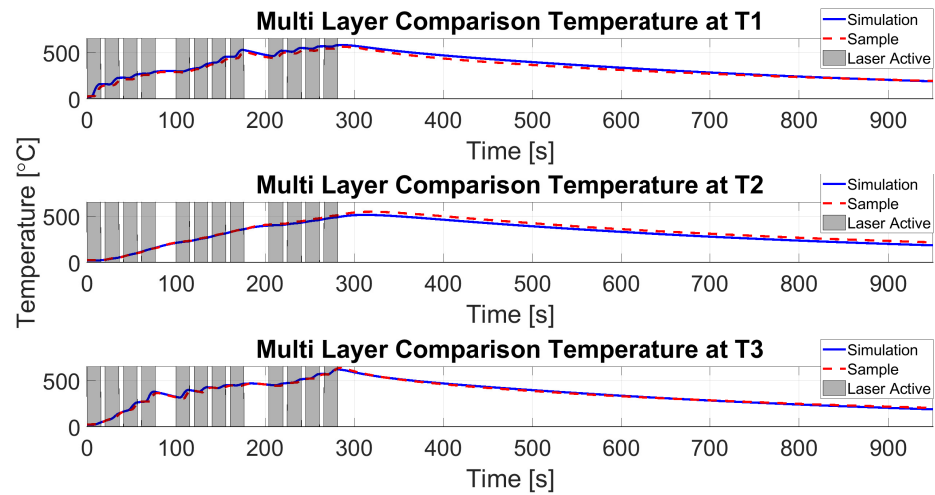


(b) Displacement history

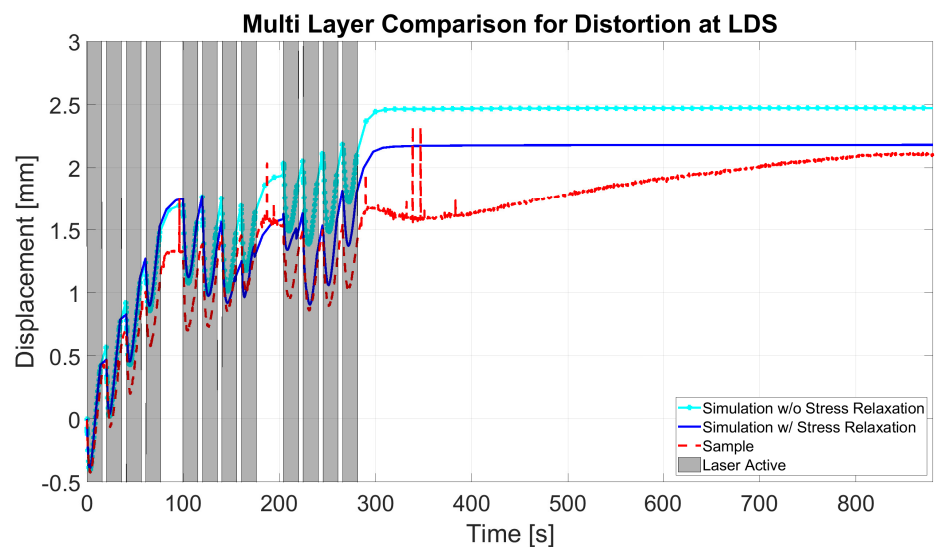
**Figure 7.** Single-layer prediction versus experimental measurements, where the coefficient of laser absorptivity  $\eta = 0.19$  and the convection coefficient =  $35 \text{ W}/(\text{m}^2 \text{ K})$ : (a) temperature history at T1–T3 and (b) displacement history at LDS. The gray shaded areas indicate the laser-active time in depositing each bead.

### 3.2. Multiple Layers

Figure 8a shows the FE predicted temperature histories at TC1–TC3 compared to the in situ measurements for a multilayer sample. It can be seen that the temperature predictions have good agreement with the measurements. The maximum percentage of error for temperature prediction is less than 6% (see Table 10).



(a) Temperature history



(b) Displacement history

**Figure 8.** Multilayer prediction versus experimental measurements, where the coefficient of laser absorptivity  $\eta = 0.19$  and the convection coefficient =  $35 \text{ W}/(\text{m}^2 \text{ K})$ : (a) temperature history at T1–T3 and (b) displacement history at LDS. The gray shaded areas indicate the laser-active time in depositing each bead.

**Table 10.** FE prediction errors in temperature and distortion.

Build Case	TC1 Max % Error	TC2 Max % Error	TC3 Max % Error	Final Distortion % Error
Single-layer	3%	5%	5%	12%
Multilayer	3%	6%	2%	3.6%

Figure 8b shows the substrate displacement histories at the LDS location predicted by the FE models with and without considering stress relaxation at 500 °C and above. It can be observed that the measured displacement undergoes an oscillating cycle, corresponding to the heating of each individual laser pass, followed by inter-pass cooling. There is a clear upward displacement during the interlayer dwell time. It is interesting to observe that the measured displacement during the dwell after layer 2 is comparable to the peak displacement after layer 1, with only a marginal increase, while the displacement after layer 3 is close to the displacement after layer 2; that is, there is little accumulation of distortion from layer to layer. The marginal accumulation of distortion from layer to layer exhibited during processing NAB may be attributed to stress relaxation caused by the phase transformations, as discussed in Section 2.4.3.

Figure 8b shows that the displacement curves predicted by the two FE models (with and without stress relaxation) almost overlap for the first layer, with both simulations capturing the oscillating cycles in the displacement corresponding to individual laser passes. The two FE-predicted displacement curves start to diverge slightly during the deposition of the second layer, with clear disparity starting from the dwell time after the second layer. The steady-state value of the FE-predicted displacement without including the stress relaxation is about 20% higher than the FE prediction with stress relaxation. The prediction error of the FE model with stress relaxation for the final distortion is less than 4% (see Table 10).

### 3.3. Runtime

The FE simulations were run using a computer of ten cores and 3.7 GHz with a peak RAM of 128 GB. The CPU runtime for the single-layer simulation model was 334 s, while for the multilayer simulation it was 681 s.

## 4. Conclusions

This paper has presented a thermomechanical analysis and validation for LHW directed energy deposition of NAB. Our analysis includes models both with and without incorporation of stress relaxation due to phase transformation. Experimental validation is conducted through in situ measurements of temperature histories at multiple locations on the substrate and of the vertical displacement at the free end of the substrate clamped along one side during deposition of single-layer and multilayer parts. The FE model parameters are first determined by matching the temperature predictions for the single-layer coupon; the resulting model is then used to predict the vertical displacement at the free end of the substrate for single-layer deposition and to generate thermomechanical simulations for multilayer deposition.

The maximum prediction errors for temperature histories are less than or equal to 6% for both the single-layer and multilayer depositions. Experimental measurements show that there is little accumulation of distortion from layer to layer during multilayer NAB deposition, which could be attributed to the phase transformations at and above 500 °C. For single-layer deposition, there is a negligible difference in predicted substrate distortions between the two FE models with and without accounting for stress relaxation, with both models having final prediction errors of about 12%. However, for multilayer deposition it is critical to add a stress relaxation at 500 °C and above in the FE model to ensure that the resulting mechanical prediction reflects the trend of marginal distortion accumulation across layers observed in the experimental measurements. This brings the final distortion prediction errors below than 4%. Further improvement of mechanical analysis to reduce prediction errors, including more sophisticated approaches in modeling the stress relaxation, will be considered in future work. Although the available experimental results show minimal sample variability, we acknowledge the limited number of repeated experiments in this study; our future work will include an increased number of repeated experiments and subsequent statistical analysis. In addition, thermomechanical analysis

for additive manufacturing of other materials exhibiting phase transformation will be considered in future work.

**Author Contributions:** Conceptualization, G.W.H., E.R. and Q.W.; methodology, G.W.H., E.R. and Q.W.; software, G.W.H.; validation, G.W.H.; formal analysis, G.W.H., E.R. and Q.W.; investigation, G.W.H.; resources, E.R.; data curation, G.W.H.; writing—original draft preparation, G.W.H.; writing—review and editing, E.R. and Q.W.; visualization, G.W.H.; supervision, E.R. and Q.W.; project administration, E.R. and Q.W.; funding acquisition, Q.W. All authors have read and agreed to the published version of the manuscript.

**Funding:** This work was supported in part by the U.S. National Science Foundation under Grant No. 2015930.

**Data Availability Statement:** The original contributions presented in the study are included in the article, further inquiries can be directed to the corresponding author.

**Acknowledgments:** The authors are grateful for the assistance of Evan West and Matthew Pantano from the Penn State Applied Research Lab for providing process descriptions, parameters, descriptions of the LHW DED system, and assistance in monitoring and depositing the NAB materials used in this work.

**Conflicts of Interest:** The authors declare no conflicts of interest.

## References

1. Imran, M.M.; Che Idris, A.; De Silva, L.C.; Kim, Y.B.; Abas, P.E. Advancements in 3D Printing: Directed Energy Deposition Techniques, Defect Analysis, and Quality Monitoring. *Technologies* **2024**, *12*, 86. [\[CrossRef\]](#)
2. Pangsrivini, S.; McGuffin-Cawley, J.; Quinn, R.; Narayanan, B.; Zhang, S.; Denney, P. Calculation of energy balance and efficiency in Laser Hot-Wire (LHW) cladding process. In Proceedings of the 2016 International Symposium on Flexible Automation (ISFA), Cleveland, OH, USA, 1–3 August 2016; IEEE: New York, NY, USA, 2016; pp. 217–222.
3. Halder, R.; Pistorius, P.C.; Blazanin, S.; Sardey, R.P.; Quintana, M.J.; Pierson, E.A.; Verma, A.K.; Collins, P.C.; Rollett, A.D. The effect of interlayer delay on the heat accumulation, microstructures, and properties in laser hot wire directed energy deposition of Ti-6Al-4V single-wall. *Materials* **2024**, *17*, 3307. [\[CrossRef\]](#) [\[PubMed\]](#)
4. Shiqing, Z.; Peng, W.; Zhenhua, F.; Jiguo, S. Numerical simulation of wire temperature field for prediction of wire transfer stability in laser hot wire welding. In Proceedings of the International Congress on Applications of Lasers & Electro-Optics, Miami, FL, USA, 7 October 2013; AIP Publishing: Melville, NY, USA, 2013; pp. 294–301.
5. Peng, W.; Jiguo, S.; Shiqing, Z.; Gang, W. Control of wire transfer behaviors in hot wire laser welding. *Int. J. Adv. Manuf. Technol.* **2016**, *83*, 2091–2100. [\[CrossRef\]](#)
6. Huang, Z.; Wang, G.; Wei, S.; Li, C.; Rong, Y. Process improvement in laser hot wire cladding for martensitic stainless steel based on the Taguchi method. *Front. Mech. Eng.* **2016**, *11*, 242–249. [\[CrossRef\]](#)
7. Liu, S.; Liu, W.; Harooni, M.; Ma, J.; Kovacevic, R. Real-time monitoring of laser hot-wire cladding of Inconel 625. *Opt. Laser Technol.* **2014**, *62*, 124–134. [\[CrossRef\]](#)
8. Zhang, Z.; Kong, F.; Kovacevic, R. Laser hot-wire cladding of Co-Cr-W metal cored wire. *Opt. Lasers Eng.* **2020**, *128*, 105998. [\[CrossRef\]](#)
9. Tyralla, D.; Seefeld, T. Higher deposition rates in laser hot wire cladding (LHWC) by beam oscillation and thermal control: Erhöhung der Abschmelzleistung beim Laser-Heißdrahtbeschichten mittels Strahloszillation und temperaturbasierter Regelung. In *Production at the Leading Edge of Technology, Proceedings of the 9th Congress of the German Academic Association for Production Technology (WGP), Hamburg, Germany, 30 September–2 October 2019*; Springer: Berlin/Heidelberg, Germany, 2019; pp. 401–409.
10. Akbari, M.; Ding, Y.; Kovacevic, R. Process development for a robotized laser wire additive manufacturing. In Proceedings of the International Manufacturing Science and Engineering Conference, Zhuhai, China, 11–12 March 2017; American Society of Mechanical Engineers: New York, NY, USA, 2017; Volume 50732, p. V002T01A015.
11. Ding, Y.; Akbari, M.; Kovacevic, R. Process planning for laser wire-feed metal additive manufacturing system. *Int. J. Adv. Manuf. Technol.* **2018**, *95*, 355–365. [\[CrossRef\]](#)
12. Nie, Z.; Wang, G.; McGuffin-Cawley, J.D.; Narayanan, B.; Zhang, S.; Schwam, D.; Kottman, M.; Rong, Y.K. Experimental study and modeling of H13 steel deposition using laser hot-wire additive manufacturing. *J. Mater. Process. Technol.* **2016**, *235*, 171–186. [\[CrossRef\]](#)
13. Liu, W.; Ma, J.; Liu, S.; Kovacevic, R. Experimental and numerical investigation of laser hot wire welding. *Int. J. Adv. Manuf. Technol.* **2015**, *78*, 1485–1499. [\[CrossRef\]](#)
14. Liang, L.; Hu, R.; Wang, J.; Huang, A.; Pang, S. A thermal fluid mechanical model of stress evolution for wire feeding-based laser additive manufacturing. *J. Manuf. Process.* **2021**, *69*, 602–612. [\[CrossRef\]](#)
15. Yao, M.; Kong, F.; Tong, W. A 3D finite element analysis of thermally induced residual stress distribution in stainless steel coatings on a mild steel by laser hot wire cladding. *Int. J. Adv. Manuf. Technol.* **2023**, *126*, 759–776. [\[CrossRef\]](#)

16. Arcos, C.; Ramos-Grez, J.; Sancy, M.; La Fé-Perdomo, I.; Setchi, R.; Guerra, C. Suitability of nickel aluminium bronze alloy fabricated by laser powder bed fusion to be used in the marine environment. *Corros. Sci.* **2024**, *226*, 111656. [[CrossRef](#)]
17. Orzolek, S.M.; Semple, J.K.; Fisher, C.R. Influence of processing on the microstructure of nickel aluminum bronze (NAB). *Addit. Manuf.* **2022**, *56*, 102859. [[CrossRef](#)]
18. Morshed-Behbahani, K.; Bishop, D.P.; Nasiri, A. A review of the corrosion behavior of conventional and additively manufactured nickel-aluminum bronze (NAB) alloys: Current status and future challenges. *Mater. Horiz.* **2023**, *10*, 5391–5435. [[CrossRef](#)]
19. Cai, X.; Yang, M.; Rui, Y.; Wang, Z.; Zhou, J.; Xue, F. Investigation of mechanical and corrosion behavior of multi-pass nickel-aluminum bronze fabricated through wire-arc directed energy deposition. *Addit. Manuf.* **2024**, *80*, 103967. [[CrossRef](#)]
20. Xu, C.; Peng, Y.; Chen, L.Y.; Chen, Z.W.; Zhang, T.Y.; Cheng, J.J.; Wang, K.H. Tailoring microstructure via heat treatment to improve the corrosion resistance of directed energy deposited nickel-aluminum bronze alloy. *J. Mater. Res. Technol.* **2023**, *25*, 5210–5226. [[CrossRef](#)]
21. Shakil, S.I.; Dharmendra, C.; Shalchi-Amirkhiz, B.; Mohammadi, M.; Haghshenas, M. Interplay between microstructure, micromechanical, and tensile properties in wire arc additive manufactured nickel-aluminum bronze: As-built and heat treated. *Materialia* **2023**, *32*, 101919. [[CrossRef](#)]
22. Hatala, G.W.; Wang, Q.; Reutzler, E.W.; Fisher, C.R.; Semple, J.K. A thermo-mechanical analysis of laser hot wire additive manufacturing of NAB. *Metals* **2021**, *11*, 1023. [[CrossRef](#)]
23. B150/B150M-19; Standard Specification for Aluminum Bronze Rod, Bar, and Shapes. ASTM International: West Conshohocken, PA, USA, 2019.
24. C95800; Class: Bronzes, Copper-Aluminum-Iron and Copper-Aluminum-Iron-Nickel Alloys (Aluminium Bronzes). The Copper Development Association Inc.: McLean, VA, USA, 2020.
25. Foteinopoulos, P.; Papacharalampopoulos, A.; Stavropoulos, P. On thermal modeling of Additive Manufacturing processes. *CIRP J. Manuf. Sci. Technol.* **2018**, *20*, 66–83. [[CrossRef](#)]
26. Goldak, J.; Chakravarti, A.; Bibby, M. A new finite element model for welding heat sources. *Metall. Trans. B* **1984**, *15*, 299–305. [[CrossRef](#)]
27. Pisarek, B. Model of Cu-Al-Fe-Ni Bronze Crystallization. *Arch. Foundry Eng.* **2013**, *13*, 72–79. [[CrossRef](#)]
28. Brezina, P. Heat treatment of complex aluminium bronzes. *Int. Met. Rev.* **1982**, *27*, 77–120. [[CrossRef](#)]
29. Dai, H.; Francis, J.; Withers, P. Prediction of residual stress distributions for single weld beads deposited on to SA508 steel including phase transformation effects. *Mater. Sci. Technol.* **2010**, *26*, 940–949. [[CrossRef](#)]
30. Denlinger, E.R.; Michaleris, P. Effect of stress relaxation on distortion in additive manufacturing process modeling. *Addit. Manuf.* **2016**, *12*, 51–59. [[CrossRef](#)]
31. Michaleris, P. Modeling metal deposition in heat transfer analyses of additive manufacturing processes. *Finite Elem. Anal. Des.* **2014**, *86*, 51–60. [[CrossRef](#)]
32. Gouge, M.F.; Heigel, J.C.; Michaleris, P.; Palmer, T.A. Modeling forced convection in the thermal simulation of laser cladding processes. *Int. J. Adv. Manuf. Technol.* **2015**, *79*, 307–320. [[CrossRef](#)]
33. Li, C.; Denlinger, E.R.; Gouge, M.F.; Irwin, J.E.; Michaleris, P. Numerical verification of an Octree mesh coarsening strategy for simulating additive manufacturing processes. *Addit. Manuf.* **2019**, *30*, 100903. [[CrossRef](#)]

**Disclaimer/Publisher’s Note:** The statements, opinions and data contained in all publications are solely those of the individual author(s) and contributor(s) and not of MDPI and/or the editor(s). MDPI and/or the editor(s) disclaim responsibility for any injury to people or property resulting from any ideas, methods, instructions or products referred to in the content.